Statistical Models for Averaging of the Pump–Probe Traces: Example of Denoising in Terahertz Time-Domain Spectroscopy

Maksim Skorobogatiy, *Senior Member, IEEE*, Jayesh Sadasivan, and Hichem Guerboukha, *Graduate Member, IEEE*

***Abstract*—In this paper, we first discuss the main types of noise in a typical pump–probe system, and then focus specifically on terahertz time domain spectroscopy (THz-TDS) setups. We then introduce three statistical models for the noisy pulses obtained in such systems, and detail rigorous mathematical algorithms to denoise such traces, find the proper averages, and characterize various types of experimental noise. Finally, we perform a comparative analysis of the performance, advantages, and limitations of the algorithms by testing them on the experimental data collected using a particular THz-TDS system available in our laboratories. We conclude that using advanced statistical models for trace averaging results in fitting errors that are significantly smaller than those obtained with only a simple statistical average.**

***Index Terms*—Error reduction, noise, pump–probe experiments, terahertz radiation, time-domain spectroscopy.**

I. Introduction

THE pump–probe technique has received a widespread use in a number of physical and engineering fields, including ultrafast spectroscopy of chemical reactions [1], nanomaterials [2], semiconductor materials [3], time-resolved microscopy [4]–[6], time-resolved magneto-optic Kerr effect [7], and most recently in THz spectroscopy. Within this technique, a laser beam (pump) is used to excite a sample, and a time-delayed laser beam (probe) interacts with the excited sample, thus probing it at various precisely controlled temporal moments. The pump and the probe can be from the same source or from two different sources. A net result of the pump–probe technique is a collection of the temporary resolved pulses that represent dynamics of a studied physical process. While all the pulses contain identical physical information, each one of them also includes a noise contribution that is unique for each pulse. The question then is how to properly average the measured time traces and their spectra in order to extract the physical information and mitigate noise. A measure of effectiveness of a given statistical approach can be, for example, the value of a signal-to-noise ratio (SNR).

Manuscript received November 14, 2017; revised January 29, 2018; accepted February 22, 2018. Date of publication April 2, 2018; date of current version May 1, 2018. *(Corresponding author: Maksim Skorobogatiy.)*

The authors are with the Department of Engineering Physics, Polytechnique de Montreal, Montréal, QC H3C 3A7, Canada (e-mail: maksim.skorobogatiy@polymtl.ca; jayesh.sadasivan@polymtl.ca; hichem.guerboukha@polymtl.ca).

Color versions of one or more of the figures in this paper are available online at http://ieeexplore.ieee.org.

Digital Object Identifier 10.1109/TTHZ.2018.2814820

II. Standard Treatment of the Pump–Probe Data

There have been various methods, both mathematical and experimental to characterize and optimize the noise and enhance the SNR for measurements obtained from a pulse–probe experiment. For example, in [8], averaging of the signal was done using two different methods—slow scanning (modulated pump/synchronous probe demodulation) and fast scanning (unmodulated pump) on a semiconductor film and a mathematical model was developed to analytically describe the SNR of the measurements. Research has also been conducted into identification and classification of noise patterns in kilohertz frequency pump–probe experiments [9]. There are also many instances for characterization and optimization of noise levels in a THz time domain pump–probe setup. In [10], Jepsen *et al.* showed a quantitative criterion to determine the frequency-dependent dynamic range. Naftaly *et al.* in [11] and [12] have shown the effects of noise in measurements using a THz-TDS system and suggested some practical measures in calibrating the experimental set-up and eliminating the noise. Several advanced models were introduced to reduce the noise in a context of material parameter extraction [13]–[16]. In such models, the denoising is directly performed on a target material parameter. Effects of different types of noise affecting the PCA antennas including the laser fluctuations, thermal noise, etc., have been discussed in [17] along with practical measures to mitigate them. Denoising algorithm involving wavelet transforms have also been used to reduce the noise levels of measurements from the THz-TDS set-ups which can enhance the SNR of the measurements [18]–[21]. Most of the statistical methods have been developed and verified only for specific applications, for example, in [20], digital signaling process have been utilized to denoise the data obtained from a THz pulsed imaging system for biological samples. It has been shown that the SNR can also be enhanced by using the terahertz differential time domain spectroscopy (TDS) technique rather than the normal method for liquids [22] or thin films [23]–[25]. In terahertz TDS (THz-TDS) setups that employ electro-optic crystals for generation and detection of THz beams, it has been shown that SNR can be enhanced by reducing distortion in the system by using quarter wave plate to increase the initial birefringence of the probe beam [26].

The goal of this paper is to revisit some of the common types of noise encountered in pump–probe experiments, and try to counter them with general mathematical models that are nonspecific to the physical nature of the studied systems. Surprisingly, such analysis has not been reported so far, to our knowledge. As we show in the following, our analysis not only allows dramatic enhancement in the SNR of the pump probe measurements, but it also allows monitoring slow time variations in the key experimental parameters such as power, phase, and jitter. Before we get into details of our approach, we remind the reader the basics of statistical analysis of the pump–probe data.

The most straightforward way of treating a collection of pump–probe pulses is to take a simple average of the pulse spectra $E_p(\omega)$ assuming that the noise contribution is a tracewise random variable with a zero mean and a standard deviation that decreases with an increasing number of traces. Then, given the spectra of a nominal pulse $E_{\mathrm{sa}}(\omega)$ (sa stands for "simple average") that describes the physical process studied by the pulse–probe technique, spectrally dependent standard deviation of the noise $\delta E_{\mathrm{sa}}^2(\omega)$, and a corresponding frequency-dependent signal-to-noise ratio $\mathrm{SNR}_{\mathrm{sa}}(\omega)$ we write the following:

$$E_{\mathrm{sa}}(\omega) = \frac{1}{N_t}\sum_{p=1}^{N_t} E_p(\omega) \tag{1}$$

$$\delta E_{\mathrm{sa}}^2(\omega) = \frac{1}{N_t}\sum_{p=1}^{N_t} |E_p(\omega) - E_{\mathrm{sa}}(\omega)|^2 \tag{2}$$

$$\mathrm{SNR}_{\mathrm{sa}}(\omega) = \frac{E_{\mathrm{sa}}(\omega)}{\sqrt{\delta E_{\mathrm{sa}}^2(\omega)}} \tag{3}$$

where N_t is the number of experimental traces. Here, SNR is defined to characterize the quality of the fit, and therefore it depends strongly on the choice of the fitting model. More precisely, it characterizes average deviation of the measured traces from the nominal (fitted) one in frequency domain. It must not be confused with the dynamic range which is defined as a ratio between the maximal signal value (over all frequencies) and the noise floor (typically inferred from the signal level at higher frequencies). In fact, as we detail in the following, SNR is generally smaller than the dynamic range as it integrates both "slow" and "fast" noise contributions, while dynamic range is mostly indicative of the "fast" noise. We note that expressions (1) and (2) can be obtained by solving a certain minimization problem. Indeed, assuming that the spectra of the individual traces are related to that of the nominal pulse $E_{\mathrm{sa}}(\omega)$ and a trace-dependent noise $\delta E_p(\omega)$ as follows:

$$E_p(\omega) = E_{\mathrm{sa}}(\omega) + \delta E_p(\omega). \tag{4}$$

expressions (1) and (2) can be obtained by minimizing the following weighting function with respect to the spectrum of the nominal pulse:

$$\begin{aligned} Q &= \frac{1}{N_t}\sum_{p=1}^{N_t}\frac{1}{N_\omega}\sum_{n=1}^{N_\omega}|\delta E_p(\omega_n)|^2 \\ &= \frac{1}{N_t}\sum_{p=1}^{N_t}\frac{1}{N_\omega}\sum_{n=1}^{N_\omega}|E_p(\omega_n) - E_{\mathrm{sa}}(\omega_n)|^2 \end{aligned} \tag{5}$$

where N_ω is the number of frequencies in the spectra of experimental pulses, which are computed using discrete Fourier transform. From (2) it also follows that the value of Q corresponds to the spectral average of noise $Q = \frac{1}{N_\omega}\sum_{n=1}^{N_\omega}\delta E_{\mathrm{sa}}^2(\omega_n)$. In practical terms, minimization of Q with respect to the complex spectra of the nominal pulse $E_{\mathrm{sa}}(\omega)$ entails solution of the following system of N_ω equations:

$$\min_{E_{\mathrm{sa}}} Q \Leftrightarrow \frac{\partial Q}{\partial E_{\mathrm{sa}}^*(\omega_n)} = 0, \quad n = 1,\ldots,N_\omega. \tag{6}$$

The main disadvantage of this algorithm and the underlying analytical fitting model (4) is the assumption that the main source of noise is in the form of an additive linear contribution to the nominal signal, and that such contribution has a zero tracewise average. In fact, one has to recognize that there are several sources of noise in a typical pump–probe system. Moreover, these sources of noise do not contribute in a linear additive fashion, and, therefore, cannot be accounted for using simple fitting models like (4). Furthermore, many other empirical trace fitting models can be employed. For example, before simple averaging, one could first superimpose the measured traces in a time domain. However, such ad hoc models do not offer a consistent interpretation of the physical origin of the registered noise, nor it is clear what the fitted trace corresponds to.

The purpose of this paper is, first, to establish the main types of noise contribution in a typical pump–probe system, then introduce several realistic fitting models for the pulses obtained in such systems, as well as mathematical algorithms to find the fitting parameters, and finally investigate the performance of such algorithms and their limitations. Without the loss of generality, an in order to make our discussion more concrete, we apply the developed algorithms to denoising of data obtained using a standard THz-TDS system (see in Fig. 1), which is a particular realization of the pump–probe experiment.

III. Sources of Noise in a Typical Pump–Probe System

In order to develop more advanced fitting models for the data obtained in a pump–probe experiment, we have to establish the main sources of noise in such systems. Without the loss of generality, we detail our algorithms using the THz-TDS system as an example. The THz-TDS, in its classical form, can be considered as a pump–probe method, where the pump and the probe lines correspond to the emitter and detector lines. In what follows, we present a rather general justification for the noise contributions in terms of the additive and multiplicative terms, and, therefore, our algorithm can be easily adapted to other pump–probe techniques. For example, the time-resolved THz spectroscopy technique [27], where an additional optical beam is used to pump the sample, is also a pump–probe system where our algorithm is applicable.

Schematic of a classic THz-TDS system is shown in Fig. 1. There, an ultrafast femtosecond laser emits a near-infrared (NIR) beam, which is furthermore divided into two beams using a 50:50 beam-splitter. The first NIR beam is then incident onto a photoconductive emitter antenna. An ac voltage source is

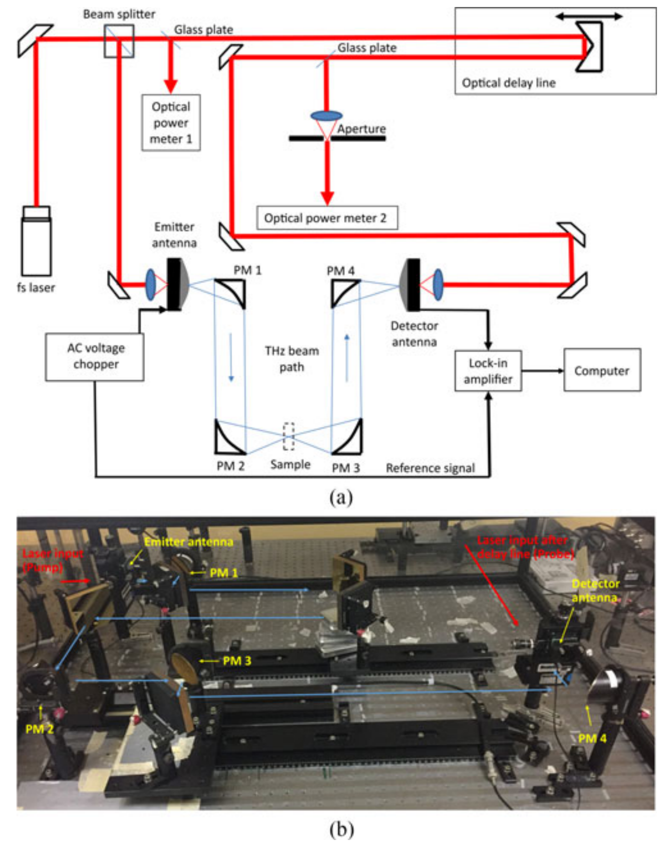

Fig. 1. (a) Schematic and (b) photograph of the THz-TDS setup.

connected to the emitter antenna acting as an electric modulator of the emitted THz beam. In other implementations, a dc voltage source is used with an emitter antenna, while a mechanical chopper is employed to interrupt the NIR beam, and thus modulate the emitted THz beam. The generated THz beam is then collimated and focused using a pair of parabolic mirrors. After interacting with a sample, the THz beam is focused onto a photoconductive detector antenna. The second NIR beam is used to excite the detector antenna after passing through a variable optical delay line. The optical delay line allows the THz pulse to be measured as a function of time by delaying the second NIR beam which gates the detector antenna. Furthermore, the THz pulse is recorded using a lock-in amplifier whose reference frequency is set by the ac voltage source (or the mechanical chopper) that modulates the emitter antenna. The measured data are essentially a current that is proportional to the electric field [16]. During the experiment, we measure both the real $E_x(t)$ and imaginary $E_y(t)$ parts of the THz pulses, which are read at the "*X*" and "*Y*" output channels of the lock-in amplifier. These components describe the relative phase between the detected signal and the reference gating and they do not have an explicit physical meaning related to the THz pulse. Variations in the relative phase are relatively slow and can typically be attributed to the temporal stability of the lock-in electronics. However, in a THz measurement, it is still desirable to acquire both channels, because the relative phase is generally nonzero and time variant, meaning that there is a nonnegligible portion of the signal that may be in the $E_y(t)$ component. While some lock-in amplifiers have an auto-phase function that helps reduce the imaginary component, in what follows, we do not consider a prior knowledge of the value of the relative phase. Therefore, the following algorithms that we present consider a total complex THz trace obtained using $E(t) = E_x(t) + iE_y(t)$.

Finally, we also monitor the time variation of the laser power, as well as variation of the optical power after the delay line by using thin glass plates to divert a small portion of the laser beam into optical power meters 1 and 2. These two measurements are useful in order to assure proper laser operation and proper optical alignment of various optical components during the measurements.

A result of a single complete measurement using a THz-TDS system with (or without) a sample inside is a temporally resolved transmitted THz pulse. In fact, when performing a careful spectroscopic study, in addition to using a relatively large averaging time constant (10–1000 ms) of the lock-in amplifier, one also acquires a relatively large number (10–1000) of pulses to further mitigate the noise. In fact, the use of a lock-in amplifier and proper averaging of the time traces serve two different purposes. Thus, the analog averaging performed by the lock-in amplifier is meant to reduce the contribution from a fast-varying noise coming mostly from various electronic and optoelectronic components, therefore larger values of a time constant are desired to reduce such noise. At the same time, a complete pulse measurement using lock-in amplifier has to be fast enough compared to the time scales set by other slow-varying processes in a system like antenna aging, laser power variation, or changes in the environmental conditions like humidity and temperature that happen on a scale of minutes to hours. Therefore, the lock-in time constant cannot be too large. Ideally, with the proper choice of a lock-in time averaging constant, individual time pulses should feature only a small contribution from the fast variable electronic noise, while they could be considered as acquired at constant environmental and experimental conditions.

In order to mitigate the effects of a slow-varying noise caused by the drift of various experimental parameters mentioned above, one typically resorts to acquiring a relatively large number of pulses that should be properly averaged to extract a desired physical information. Due to the fact that over time of a standard experiment (hours–days), time average of many slow-varying parameters is not zero, simple averaging of traces as given by (1) will not be efficient in mitigating this type of "slow" noise. Therefore, system-specific fitting functions must be introduced in order to compensate for the slow-varying trace-to-trace drifts of various experimental parameters.

We now investigate in more details the pump–probe system presented in Fig. 1 and identify the principle sources of noise in such systems. First, we note that the average power of an fs laser varies over time. A time-resolved measurement using optical meter of a Menlo C-Fiber 780 Femtosecond Erbium laser shows $\sim$1% variation on a 60 min time scale, which could affect the THz pulse amplitude. Additionally, the photoconductive antennas used for THz generation age over time resulting in lower emitted power under the same excitation conditions, which will again affect the THz pulse amplitude. In our case, due to the all the above-mentioned causes, we estimate $\sim$10% variation in the detected power over 24 h of continuous use.

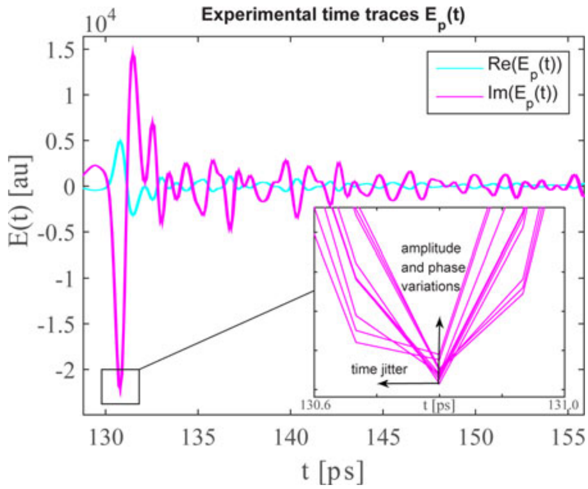

Fig. 2. Example of the experimental THz traces with various types of noise identified.

Moreover, when measuring THz pulse transmission under ambient not temperature stabilized conditions, humidity variation causes changes in the THz absorption (pulse amplitude), while temperature variation causes changes in the pulse phase and propagation time due to drifts in the setup physical dimensions, as well as refractive indices of various optical elements. The time scale for such variations in the environmental conditions in our lab is $\sim$1 h. Finally, we note that the optical delay line used in our experiments introduces an addition trace-to-trace variation in the pulse position. This is related to the fact that a typical optical delay line uses a retroreflector mirror mounted onto a linear micropositioning stage that show variation and drift in its absolute position during repetitive use. Particularly, in our lab we use a Newport delay line that is specified for 1.5 μm (unidirectional) precision repeatability in the absolute position of the delay line, which amounts to 0.01 ps trace-to-trace variation in the position of the pulse. As an example, in Fig. 2 we plot the result of a typical THz-TDS measurement of an empty system. We present ten consecutively acquired THz pulses and notice three major types of trace-to-trace variations which are pulse amplitude, pulse phase, and pulse position (pulse jitter) variations.

In what follows, we present three different analytical models that take into account the three abovementioned types of "slow" noise that include pulse power and phase variations, as well as pulse jitter. The three models are different in the way they include the leftover "fast" noise which is not completely compensated by the lock-in amplifier. We then detail mathematical formulation for fitting experimental data using the proposed analytical models. Finally, we perform a comparative analysis for the quality of the extracted data by comparing results of simple averaging versus more advanced algorithms discussed in this paper.

IV. Advanced Models to Mitigate Noise in the Pump–Probe Experiments

Let us denote the nominal THz field emitted by the photoconductive antenna as $E_o(t)$. In what follows, by denoising, we mean extraction of a signal from the mixture of signal and noise given by the experimental traces. Within this definition, $E_o(t)$ can be considered as a denoised THz trace. Due to various sources of noise, like laser power and phase variation over time, imprecision in the absolute position of the optical delay line from one run to another, as well as noise incurred during beam propagation and emission/detection, the THz field of trace p detected by the receiver antenna $E_p(t)$, as well as its spectrum $E_p(\omega)$ can be written in the simplest form as follows:

Model 1:

$$\begin{aligned} E_p\left(t\right) &= C_p E_o\left(t-\delta t_p\right) + \delta E_p\left(t-\delta t_p\right) \\ E_p\left(\omega\right) &= \left(C_p E_o\left(\omega\right) + \delta E_p\left(\omega\right)\right) e^{-i\omega\delta t_p}. \end{aligned} \tag{7}$$

In the expression above, C_p are the complex gain factors of the transmission system $C_p \sim E_p/E_o$ that account for "slow" changes in the system optical properties happening between acquisition of the two consecutive traces, and that cannot be removed by a lock-in amplifier. Those include laser power variation, emitter antenna aging, changing optical path absorption, and optical path phase variation. Additionally, we introduce δt_p, which are the temporal shifts of the THz pulses due to imprecision in the absolute position of the optical delay line from one scan to another. Finally, the leftover "fast" noise which is not completely compensated by the lock-in amplifier is denoted as $\delta E_p(t)$. This noise is incurred either during pulse propagation or emission/detection and it varies on a time scale which is much faster than the time of a single measurement. Note that in model (7) we assume that the noise $\delta E_p(t)$ is independent of the pulse amplitude C_p. This is a valid assumption if the noise is purely electrical in nature and comes, for example, from the semiconductor carrier density fluctuations in the photoconductive antenna, as well as other processes that are either independent of the photoexcitation process or that happen while operating in the saturation regime of the photoexcitation process. Here, by saturation regime we mean the case when increasing laser power does not lead to increase in the THz signal intensity.

Alternatively, if the "fast" noise is generated while operating in the unsaturated regime of the photoexcitation process during pulse generation or detection (for example photoexcited carrier density fluctuations), then it is reasonable to assume that the noise should be proportional to the amplitude of the excitation laser beam. We can then write a new model for the relation between the nominal and the registered traces as follows:

Model 2:

$$\begin{aligned} E_p\left(t\right) &= C_p\left(E_o\left(t-\delta t_p\right) + \delta E_p\left(t-\delta t_p\right)\right) \\ E_p\left(\omega\right) &= C_p\left(E_o\left(\omega\right) + \delta E_p\left(\omega\right)\right) e^{-i\omega\delta t_p}. \end{aligned} \tag{8}$$

Finally, if the "fast" noise is incurred during pulse propagation due to rapidly changing environmental factors like variable air flows, sudden humidity variations, or changing air particulate density, then it is reasonable to assume that the noise should be proportional to the amplitude of the pulse itself, and we can write a third model for the relation between the nominal and the registered traces as follows:

Model 3:

$$\begin{aligned} E_p\left(t\right) &= C_p E_o\left(t-\delta t_p\right)\left(1+\delta_p\left(t-\delta t_p\right)\right) \\ E_p\left(\omega\right) &= C_p E_o\left(\omega\right) e^{-i\omega\delta t_p}\left(1+\delta_p\left(\omega\right)\right). \end{aligned} \tag{9}$$

Ideally, given an experimental data, one should be able to infer the nature of the "fast" noise by performing comparative analysis of the data using models 1–3. Particularly, if the "fast" noise is generated by the nonsaturated photoexcitation process or by the rapidly changing environmental factors, then models 2, 3 should result in the noise amplitudes δE_p, δ_p that are independent of the gain factorsC_p. At the same time, model 1 would predict noise amplitudes which are proportional to the gain factors $\delta E_p \sim C_p$. Alternatively, if the "fast" noise is generated by the saturated photoexcitation process or by electronic processes that are independent of the laser power and pulse amplitude, then model 1 should predict noise amplitudes δE_p which are independent of the gain factors C_p, while models 2, 3 should predict noise amplitudes which are inversely proportional to the gain factors $\delta E_p, \delta_p \sim 1/C_p$.

Finally, we note that although the three models differ only in the analytical representation of the "fast" noise, their mathematical treatments will be quite different from each other as we will see in what follows. In all three cases, we will find the fitting parameters by using minimization of the corresponding weighting functions that are defined to be proportional to the average value of the "fast" noise in the data.

V. Finding Parameters by Solving Optimization Problem

In order to find various fitting parameters used in the analytical forms of the fitting functions (7)–(9), we first define model-dependent "fast" noise as follows:

Model 1:

$$\delta E_p(\omega) = E_p(\omega)\, e^{i\omega\delta t_p} - C_p E_o(\omega). \tag{10}$$

Model 2:

$$\delta E_p(\omega) = a_p E_p(\omega)\, e^{i\omega\delta t_p} - E_o(\omega) \quad a_p = \frac{1}{C_p}. \tag{11}$$

Model 3:

$$\begin{aligned}&\delta_p(\omega) = \ln(E_p(\omega)) - \ln(C_p) - \ln(E_o(\omega)) + i\omega\delta t_p\\ &\delta_p(\omega) \ll 1.\end{aligned} \tag{12}$$

In order to find the complex gain factors C_p (or their inverse a_p), time shifts δt_p, and a spectrum of the nominal THz field $E_o(\omega)$ we define an optimization problem with respect to the spectrally and tracewise averaged value of the noise. In other words, we look for the values of the abovementioned fitting parameters that minimize the following weighting functions Q:

Models 1, 2:

$$Q = \frac{1}{N_t}\sum_{p=1}^{N_t}\frac{1}{N_\omega}\sum_{n=1}^{N_\omega}|\delta E_p(\omega_n)|^2. \tag{13}$$

Model 3:

$$Q = \frac{1}{N_t}\sum_{p=1}^{N_t}\frac{1}{N_\omega}\sum_{n=1}^{N_\omega}|\delta_p(\omega_n)|^2 \tag{14}$$

where N_t is the number of THz pulses used in the fitting, and N_ω is the number of frequency components in the Fourier spectrum of the measured pulses. In order to find the minimum of the weighting functions (13), (14), we have to solve a system of $N_\omega + 2N_t$ generally nonlinear equations

$$\begin{aligned}&\textit{Models 1, 2:}\ \frac{\partial Q}{\partial E_o^*(\omega_n)} = 0\\ &\textit{Model 3:}\ \frac{\partial Q}{\partial \ln(E_o(\omega_n))^*} = 0, \quad n = 1,\ldots,N_\omega\end{aligned} \tag{15}$$

$$\begin{aligned}&\textit{Model 1:}\ \frac{\partial Q}{\partial C_p^*} = 0\\ &\textit{Model 2:}\ \frac{\partial Q}{\partial a_p^*} = 0\\ &\textit{Model 3:}\ \frac{\partial Q}{\partial \ln(C_p)^*} = 0, \quad p = 1,\ldots,N_t\end{aligned} \tag{16}$$

$$\textit{Models 1, 2, 3:}\ \frac{\partial Q}{\partial \delta t_p} = 0, \quad p = 1,\ldots,N_t. \tag{17}$$

Additionally, we note that for each model, a system of equations (15)–(17) is ill-posed and does not lead to a unique solution. This is related to the fact that the analytical fitting functions (7)–(9) are degenerate with respect to certain transformations of the groups of the fitting variables as explained further in the text. Therefore, in order to obtain a unique solution to (15)–(17) we need to introduce additional constraints, which come in the form of various normalization conditions for the complex gain coefficients, as well as an assumption about the mean value of the time shifts. Furthermore, a more involved discussion is necessary in the case of model 3 due to the fact that natural logarithm of a complex function gives a complex phase defined up to an unknown 2π multiplier, thus requiring careful phase unwrapping and removal of various numerical artifacts.

Finally, we note that in the case of models 1, 2 a system of equations (15)–(17) contains $N_\omega + N_t$ linear equations (15), (16), as well as N_t nonlinear equation (17). Therefore, solution of such equations requires an iterative method which can be computationally intensive when dealing with a large number of THz traces. That said, we find that nonlinear system of equations (15)–(17) is very stable and solution can be found readily after only a few iterations of any standard iterative algorithm, like a Newton method. At the same time, model 3 results in a system of $N_\omega + 2N_t$ linear equations that can be furthermore solved in a closed form. Therefore, model 3 is considerably less numerically intensive than models 1, 2. That said, we find that model 3 is more unstable and it is more prone to noise than models 1, 2, which is a direct consequence of the need to properly unwrap phases of all the traces before using model 3. We therefore conclude that models 1, 2 are preferred when analyzing sets of pump–probe traces as they give highly stable and predictable results over all frequency regions covered by the pulse spectra. At the same time, model 3 is preferred when one needs direct access to a continuous phase of the fitted nominal trace, which is necessary when extracting effective refractive index of the propagation media, or when interpreting results of the cut-back measurements of waveguides.

Due to length and complexity of the mathematical formulation of the three algorithms we have placed them in the Appendix document found in [28]. In the following sections, we rather concentrate on the comparative analysis between the three models, while referring the reader to Appendix document [28] for mathematical details related to the fitting algorithm implementation. A MATLAB code implementation is also available in [29].

VI. Application of Models 1, 2 to Analysis of the Time Pulses

In this section, we present an example of analysis of a collection of 400 THz time traces acquired using an in-house THz-TDS system. We note that the following analysis aims only at giving an example of statistical treatment of the THz traces, while involving only a single set of pulses acquired using a particular choice of experimental parameters. Therefore, the conclusions of this analysis are not representative of all the different THz-TDS systems, neither of the different excitation and detection regimes that can be realized using such systems. We stress that in this paper we do not aim at answering the question about which model 1, 2, or 3 and in which operation regime is more applicable to represent noise in the THz-TDS systems. The aim of this paper is, rather, to introduce several plausible models for the modeling and negation of the different types of noise, while the aim of this section is to simply demonstrate the type of results that can come from such an analysis.

The experimental system features a frequency doubled Menlo C-Fiber 780 Femtosecond fiber-laser (90 fs, repetition rate of 100 MHz, wavelength of 780 nm), and the photoconductive antennas deposited on low-temperature-grown GaAs substrates (TERA8-1, Menlo Systems). Two NIR optical beams of ~10 mW power were used to excite and gate the emitter and detector antennas, while a 20 V 24 kHz ac voltage source was used to modulate the emitter antenna and the THz signal. The THz pulses were acquired using the SR830 Lock-in Amplifier (Stanford Research Systems). Experimental parameters during pulse acquisition were chosen as follows: 10 ms lock-in time constant of the amplifier, 20 μm step size of the delay line (corresponding time resolution of 0.133 ps, and a maximal frequency of 3.75 THz), a total optical delay of 100 mm (corresponding frequency resolution of 3 GHz). The acquisition time of a single THz pulse was 4 min. The delay line precision for the absolute position reproducibility was 1.5 μm (unidirectional), thus resulting in time jitter of pulses ~0.01 ps. Additionally, we have used a Newport 841 PE optical power meter to record the laser intensity before each trace measurement, as well as to record the NIR power after the delay line (see Fig. 1).

In Fig. 3, we show real (solid cyan) and imaginary parts (solid magenta) of the experimentally acquired traces $E_p(t)$, as well as real (dotted blue) and imaginary (dotted red) parts of the fitted nominal pulse $E_o(t)$ that were found using model 1 (7), and by minimizing weighting function (13). Visually, there is an excellent agreement between the experimental measurements and a theoretical fit. At the same time, we notice that some

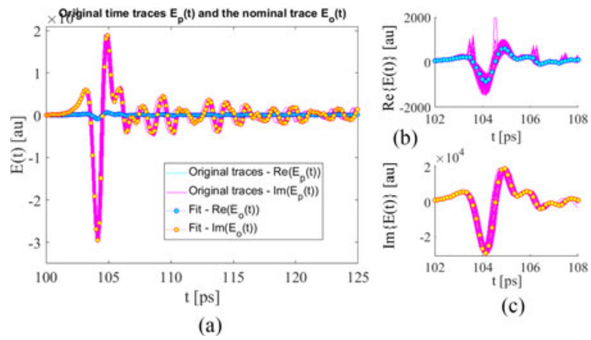

Fig. 3. (a) Experimentally measured time traces $E_p(t)$ (solid curves) and the nominal pulse fit $E_o(t)$ (dotted curves with circles). (b) Close-up of the trace real parts and (c) the imaginary parts as measured by the lock-in amplifier.

experimental traces deviate significantly from the other traces, and as we will see in the following, they are characterized by strong variation of some (or all) of their key parameters (power, phase, time shift) from the rest of the traces. This normally happens due to some unforeseen significant fluctuations in the system (like a stuck delay stage, sudden draft of air when a person passes next to a measurement setup, etc.), from which the system rapidly recovers on the following trace acquisition. It is normally a good idea to remove such traces from the further analysis as they are not representative of the trace ensemble.

In Fig. 4(a), we plot spectra $E_p(\omega)$ of the experimental pulses (solid green), spectrum of the fitted nominal pulse $E_o(\omega)$ (solid blue), and a spectrum of the fitting error $\delta E_o(\omega)$ (solid red) defined as a tracewise average of the individual fitting errors (10)

$$\delta E_o^2(\omega) = \frac{1}{N_t} \sum_{p=1}^{N_t} |\delta E_p(\omega)|^2. \tag{18}$$

Additionally, in Fig. 4(b), we present a frequency-dependent signal-to-noise ratio $\mathrm{SNR}_o(\omega)$ for the model 1 fit defined as follows:

$$\mathrm{SNR}_o(\omega) = \frac{E_o(\omega)}{\sqrt{\delta E_o^2(\omega)}}. \tag{19}$$

For comparison, in Fig. 4 we also present spectrum of the nominal pulse $E_{\mathrm{sa}}(\omega)$ (dashed cyan) as calculated using simple averaging equation (1), an associated fitting error $\delta E_{\mathrm{sa}}(\omega)$ (dashed magenta) as calculated using (2), as well as a frequency-dependent signal-to-noise ratio $\mathrm{SNR}_{\mathrm{sa}}(\omega)$ computed for the simple average approximation according to (3).

From Fig. 4, we can see clearly that using advanced fitting model 1 results in a considerably more precise fit of the experimental data compared to the simple average approximation. Indeed, the spectrum of the fitting error $\delta E_o(\omega)$ for model 1 features values that vary in a relatively narrow range of 2–5 $\cdot\, 10^3$ a.u. throughout the whole frequency range [see Fig. 4(a)]. At the same time, the values of the fitting error $\delta E_{\mathrm{sa}}(\omega)$ for a simple average approximation are strongly frequency dependent and vary in a much larger range of 2–30 $\cdot\, 10^3$ a.u. Similarly, signal-to-noise ratio for the model

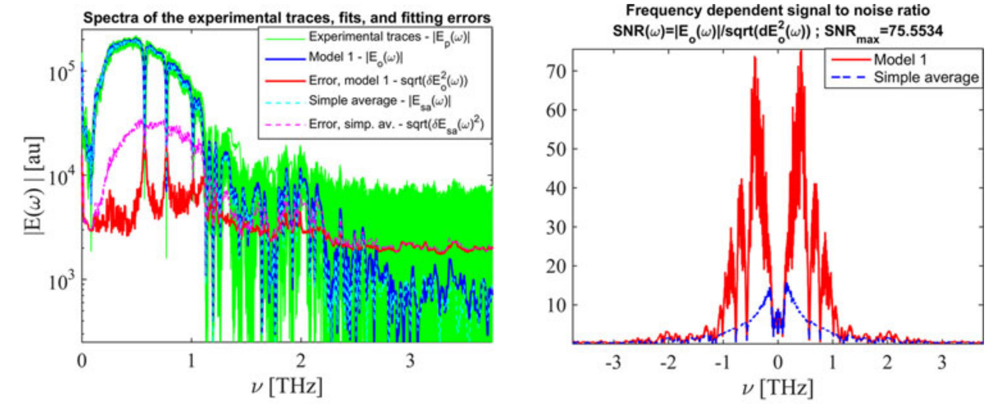

(a) (b)

Fig. 4. Comparison of the quality of the fit using model 1 versus simple average approximation. (a) Spectra of the experimental traces, those of various fits and the corresponding fitting errors. (b) Frequency-dependent signal to nose ratio for various fits.

1 is considerably higher than that for the simple average approximation at most frequencies; thus, $\mathrm{SNR}_o(\omega)$ reaches the value of ~ 75 for model 1, while the maximum $\mathrm{SNR}_{\mathrm{sa}}(\omega)$ for a simple average approximation is only ~ 15. As we have mentioned earlier, SNR depends strongly on the choice of a fitting model. Thus, for a nonoptimal model (like simple averaging) it can be much smaller than the dynamic range as it integrates both "slow" and "fast" noise contributions, while dynamic range is mostly indicative of the "fast" noise contribution. Indeed, from Fig. 4 we can infer the value of the dynamic range (by field) to be ~ 120. This value is considerably larger than the SNR related to a simple averaging model, while being comparable to the SNR in case of the advanced fitting models presented in this paper.

From Fig. 4, we also notice that in the near vicinity of the water vapor absorption lines, both the fitting error and SNR as obtained using model 1 does not show any improvements compared to those computed using simple averaging. This is related to the fact that in these spectral regions, model 1 does not capture the nature of the noise origin. In fact, in order to work properly near the water absorption lines, model 1 has to be further augmented to account for the trace-to-trace variation in the optical path absorption that can be caused, for example, by small changes in the optical path length. Although not explored in this paper, model 1 can be further improved by introducing, for example, a $e^{-i\alpha(\omega_n)\delta L_p}$ multiplier in (7), where $\alpha(\omega_n)$ is the absorption loss of water vapor during experiment, while δL_p are new fitting parameters that characterize trace-to-trace variation in the optical path length. As most of the THz-TDS experiments are conducted in a dry nitrogen environment, or the spectral data are used away from the water absorption lines, we did not pursue this issue further.

In Fig. 5, we present some of the statistical properties of traces plotted versus the trace number. As THz traces are acquired consecutively at equal time intervals (every 4 min), this statistical data essentially present variation of the trace properties as a function of time over the period of one day. For example, Fig. 5(a) presents time shifts δt_p in the THz pulse temporal position over time as fitted using model 1. From the figure, we note "fast" trace-to-trace variation in the value of time shifts on a scale of ~ 0.04 ps. This variation is directly related to the absolute position repeatability of the mechanical stage used in the optical delay line which is specified at $\delta x \gtrsim 1.5\,\mu$m, which in turn, corresponds to the uncertainty in the trace position of $\delta t \sim 2\delta x/c \gtrsim 0.01$ ps. Moreover, we observe an overall "slow" drift of the THz pulse position over time that can be as much as 0.2 ps after all 400 measurements. Next, Fig. 5(b) shows changes in the trace power over time, where trace power is defined to be proportional to the square of the gain coefficient. From the figure, we note that "fast" trace-to-trace power variation is quite small and is on the order of $\sim 1\%$. At the same time, we also note a "slow" variation of the average value of trace power, which can be as high as 10%–20% over the time scale of the whole experiment (one day). The underlying reason for such strong power variation is not quite clear as the measurements of the laser power [see inset in Fig. 5(b)] show less than 1% variation during the whole experiment (inset: power meter 1), while antenna aging effects usually lead to reduction of the THz power over time and not to the power increase as seen in Fig. 5. Most probable cause of such power variation is in the micromisalignment of various optical elements during the experiment, particularly the ones installed on the moving delay line. An indirect confirmation of this is seen in the inset (power meter 2) in Fig. 5 top right. There, we show laser intensity variation after the delay line when a portion of the laser beam is diverted and focused onto the power meter through a $100\,\mu$m aperture. This simulates variation in the power of the laser beam that is focused onto the detector antenna after an optical delay line. Strong power variations of $\sim 10\%$ were observed over the course of the measurements making us to suspect that it is the accumulation of the small trace-to-trace changes in the optical alignment or optical path quality related to the optical delay line which are responsible for large "slow" variation in the trace optical power. Another potential cause for the long-term variations in the trace power (beyond antenna aging) can be spontaneous loss of the mode locking in the laser with a consequent recovery in a somewhat different mode locking configuration. Although this power variation mechanism was indeed observed in several of our measurements, it is typically characterized by a much dramatic and sudden change in the trace power (30%–60%)

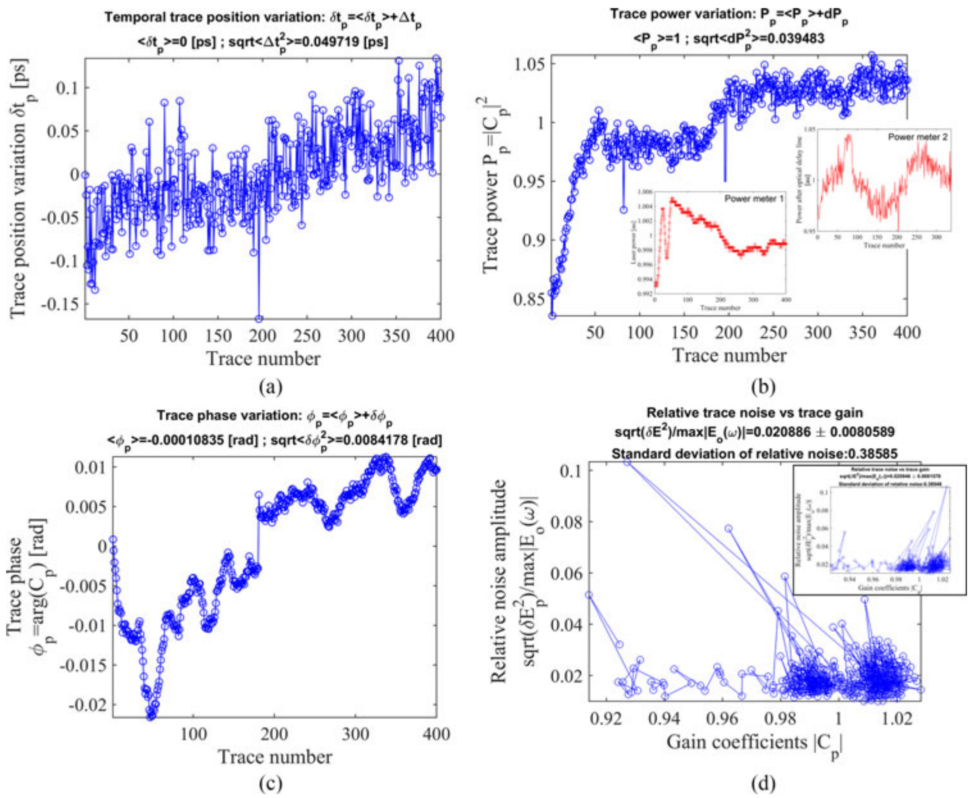

Fig. 5. Statistical analysis of 400 THz traces using model 1. (a) Trace position shift versus the trace number. (b) Trace power versus the trace number; inset 1—laser power before the optical delay line measured before acquisition of each THz pulse; inset 2—laser power after the optical delay line measured before acquisition of each THz pulse. (c) Trace phase versus the trace number. (d) Frequency averaged trace noise versus the trace number; inset—same data but obtained using model 2.

compared to 10%–20% relatively slow power change that is observed in the majority of our measurements.

Moreover, we note that the average trace power typically stays relatively constant over 10 s or even 100 s of traces, while suddenly changing to another value over a span of several measurements, which is again a testament of some permanent changes either in the optical path or the laser beam quality during the course of the experiment. We can say that in terms of power, traces can be subdivided into different clusters, each one characterized by an almost constant average power and relatively small power variation within each cluster. This clustering of the traces can also be seen in Fig. 5(c) and (d) where we show trace phase and frequency averaged trace error variations. Thus, in Fig. 5(c) we show trace phase defined as the phase of the complex gain coefficient $\arg(C_p)$, and observe that it generally varies in a relatively smooth manner from trace to trace, while exhibiting sudden jumps between different clusters of traces. The trace clustering phenomenon is particularly evident when plotting the frequency averaged fit error for each trace δE_p versus the trace gain coefficient $|C_p|$ [see Fig. 5(d)]. The frequency averaged fit error for a trace p is defined as follows:

$$\delta E_p^2 = \frac{1}{N_\omega}\sum_{n=1}^{N_\omega} |\delta E_p(\omega_n)|^2. \tag{20}$$

Finally, as we have discussed earlier, Fig. 5(d) can, in theory, provide justification for the choice of a particular noise model (7)–(9) that reflects best the nature of the "fast" noise in a pump–probe setup. For example, if the noise is independent of the trace power (model 1), then according to (7) we should expect that δE_p is also independent of $|C_p|$; at the same time, using model 2 (8), or model 3 (9) to describe the same trace set, will result in $\delta E_p \sim 1/|C_p|$ dependence. Unfortunately, when analyzing experimental data, frequently (however, not always) we cannot see statistically significant difference between the results of different models, due to large standard deviation of the noise amplitude. To demonstrate this point, in the inset in the Fig. 5(d) panel, we show results of using model 2 and observe a very similar behavior of the noise amplitude versus the trace gain coefficient as in the case of model 1. Further studies are, therefore, necessary to address this issue, which would entail comparison between the models under different power excitation/detection and environmental conditions, which is beyond the scope of this paper.

VII. Discussion of Phase Unwrapping and Model 3

Here, we discuss some fundamental problems when trying to use model 3 in data fitting. We remind the readers that if we suppose that the noise is proportional both to the pulse amplitude C_p and the nominal pulse intensity E_o, then we can write the pulse and its spectrum as in (9) as follows:

$$\begin{aligned} E_p(t) &= C_p E_o(t-\delta t_p)\left[1+\delta_p(t-\delta t_p)\right] \\ E_p(\omega) &= C_p E_o(\omega)\, e^{-i\omega\delta t_p}\left[1+\delta_p(\omega)\right] \end{aligned} \tag{21}$$

where $\delta_p(\omega)$ is the relative noise term for the pulse p. Taking natural logarithm of the pulse spectrum, and assuming that the amplitude of the relative noise is small $|\delta_p(\omega)| \ll 1$, we can rewrite (21) as follows:

$$\delta_p(\omega) = \ln(E_p(\omega)) - \ln(C_p) - \ln(E_o(\omega)) + i\omega\delta t_p. \quad (22)$$

Here, it is important to mention a fundamental problem that arises when trying to compute a natural logarithm of a complex physical property. In particular, complex spectrum of a physical pulse can be represented using its frequency-dependent absolute value and phase as $E_p(\omega) = |E_p(\omega)|e^{i\varphi_p(\omega)}$. For a physical property, like a pulse spectrum, its phase is typically a continuous function of frequency. However, when computing numerically natural logarithm of a complex, frequency-dependent function one gets the value of a "wrapped" phase confined to the $[0, 2\pi)$ interval that has a sawtooth pattern when plotted versus frequency

$$\ln(E(\omega)) = \ln(|E(\omega)|) + i \cdot \mathrm{mod}(\varphi(\omega), 2\pi). \quad (23)$$

Therefore, (22) cannot be used directly when formulating an optimization problem as it assumes that natural logarithms [used in (22)] result in true continuous phases of the functions rather than the folded ones. Therefore, in order to use (22), one has to first "unwrap" the phase found numerically using (23). An operation of phase unwrapping typically starts with a phase value φ_1 computed using (23) at the edge ω_1 of the frequency interval of interest. Then, one considers the value of the phase φ_2 computed using (23) at the adjacent frequency ω_2. One assumes that the frequency grid is dense enough so that the phase change from one frequency to another is slow so that normally $|\varphi_2 - \varphi_1| < \varepsilon_\varphi \ll 2\pi$, where ε_φ is a certain tolerance parameter. This condition, however, is broken when continuous phase $\varphi(\omega)$ reaches $|\varphi_1| \sim 2\pi$ at ω_1 and goes over 2π atω_2, which results in $|\varphi_2| \sim 0$ due to phase wrapping by (23). The phase "unwrapping" algorithms thus start at the edge of a frequency interval of interest, and then go from one frequency to another, find the 2π phase jumps caused by (23), and correct them by adding an appropriate 2π multiplier so that the resultant "unwrapped" phase $\varphi(\omega)$ is a continuous function in a sense that for any two adjacent frequencies $|\varphi(\omega_2) - \varphi(\omega_1)| < \varepsilon_\varphi$. We also note that even if the phase unwrapping is perfectly implemented, the resulting phase is still different from the true one $\varphi(\omega)$ by a constant $2\pi n$ additive factor, where n is some integer. This is because the value of the first phase at the edge of the frequency interval φ_1 can only be found up to a constant $2\pi n$ additive factor.

Yet another complication is that the realistic pulse spectra normally show strong absorption regions (water vapor absorption lines, for example), where the pulse spectral intensity can become lower than the noise level, and, consequently, the phase is scrambled. Therefore, when performing phase unwrapping, one normally finds several (N_u) disjoint frequency regions of successful phase unwrapping. We denote such frequency intervals as W_r, where $r = 1, \ldots, N_u$. We then denote N_ω^r as the number of frequencies within each interval W_r.

We now modify the fitting function (22) in order to account for the unknown $2\pi n$ additive factors that arise during phase unwrapping. Particularly, we define a phase correction function $\varphi_{p,r}$ that takes $N_t \times N_u$ values and that modifies (23) as follows:

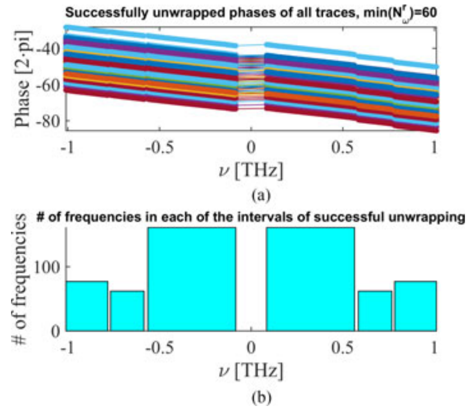

Fig. 6. (a) Unwrapped phases of all the traces. (b) Chart identifying positions of the common frequency intervals of successful phase unwrapping and a number of frequencies in each of the intervals.

$$\delta_p(\omega) = \ln(E_p(\omega)) - \ln(C_p) - \ln(E_o(\omega)) + i\omega\delta t_p + i\varphi_{p,r}, \quad \omega \in W_r. \quad (24)$$

Expression (23) means that within each interval of successful phase unwrapping W_r we have to correct for the $2\pi n_{p,r}$ shifts that were introduced when performing phase unwrapping of different traces. Similarly, in place of (22), we can write a new definition of the fitting function that is more suitable when working with logarithms of the complex functions

$$E_p(\omega) = C_p E_o(\omega) e^{-i\omega\delta t_p - i\varphi_{p,r}} [1 + \delta_p(\omega)], \quad \omega \in W_r. \quad (25)$$

VIII. Application of Model 3 to Analysis of the THz Time Traces

In this section, we analyze the same 400 THz time traces as presented earlier, but now using model 3. First step is to unwrap the frequency-dependent phase $\mathrm{Im}(\ln(E_p(\omega)))$ of each of the traces, as well as to find the common frequency intervals W_r (shared by all the traces) of successful phase unwrapping. In Fig. 6(a), we present unwrapped phases of all the traces, as well as a chart in Fig. 6(b) that identifies positions of the common frequency intervals of successful phase unwrapping and the number of frequencies in each of such intervals. During phase unwrapping, we require that each frequency interval of successful phase unwrapping contains at least $\min(N_\omega^r) = 60$ frequency points. From Fig. 6, we observe that there are $r = 6$ of such intervals. In principle, we can set $\min(N_\omega^r)$ to its lowest possible value of 2, however, the intervals containing a small number of frequencies will typically have a significant phase noise contribution, which would affect negatively the quality of the fit. Our experience tells us that the minimal value of frequencies in each interval $\min(N_\omega^r)$ should be greater than 10–20 to guarantee that the results of the fit using model 3 are consistent with those obtained using models 1 and 2. As it is evident from Fig. 6, due to the use of a complex logarithm function, the unwrapped phases of different traces feature distinct $2\pi n_{p,r}$ additive factors within each of the intervals of successful phase unwrapping. These phase

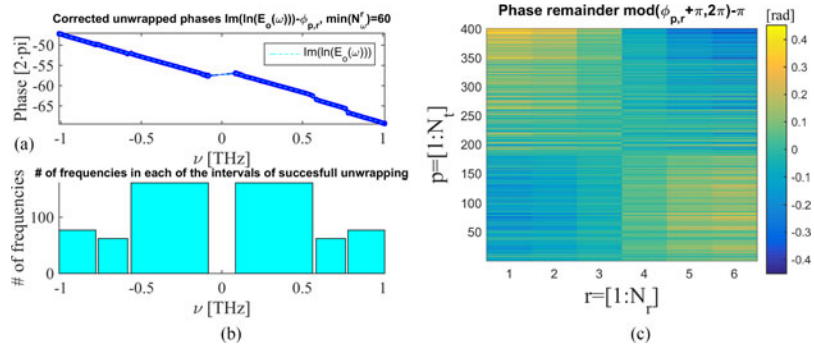

Fig. 7. (a) and (b) Unwrapped phases (as in Fig. 6) compensated with the appropriate $\varphi_{p,r}$ phase correction factors. (c) $\mathrm{mod}(\varphi_{p,r}, 2\pi)$, which is generally expected to be close to zero.

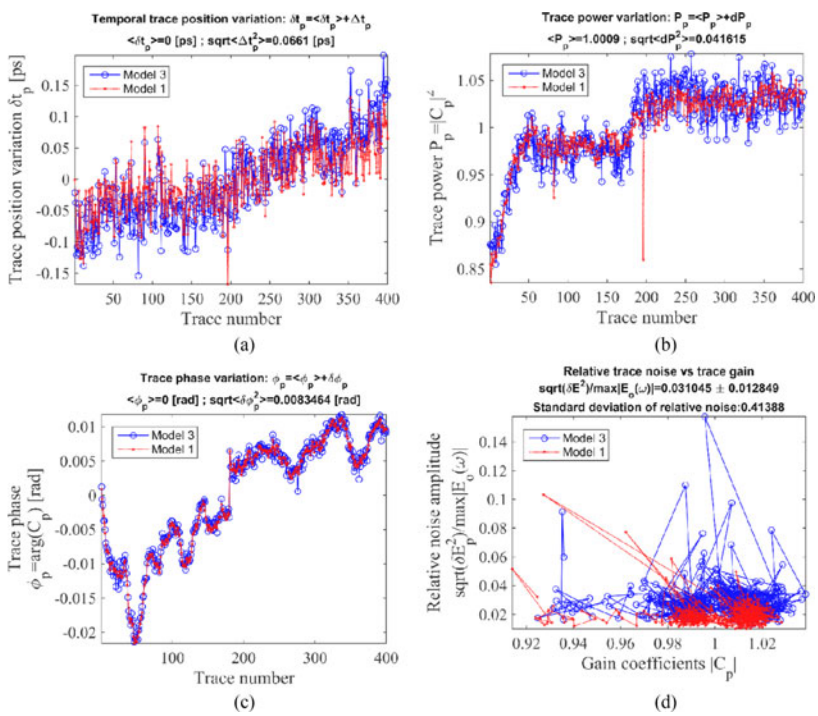

Fig. 8. Statistical analysis of 400 THz traces using model 3 (solid blue), and comparison with model 1 (dashed red). (a) Trace position shift versus the trace number. (b) Trace power versus the trace number. (c) Trace phase versus the trace number. (d) Frequency averaged trace noise versus the trace number.

shifts $\varphi_{p,r}$ $(p = 1, \ldots, 400;\ r = 1, \ldots, 6)$ can be recovered and compensated for by using a more advanced form of the fitting function (25).

Thus, in Fig. 7(a) and (b) we show the same unwrapped phases as in Fig. 6, however compensated with the appropriate $\varphi_{p,r}$ phase correction factors $\mathrm{Im}(\ln(E_p(\omega))) - \varphi_{p,r};\ \omega \in W_r$. Clearly, unwrapped phases of all the traces collapse into the same curve. While, we expect that all the $\varphi_{p,r}$ factors should be proportional to 2π, in practice we find that this only holds approximately. Thus, in Fig. 7(c), we plot $\mathrm{mod}(\varphi_{p,r}, 2\pi)$ and discover that while their absolute values are relatively small $(< 0.4\,\mathrm{rad})$, however, they are not zero.

The reason for such a behavior (as detailed in [26, Appendix III]) is in the competition between the two phase factors $\omega\delta t_p$ and $\varphi_{p,r}$ that appear in model 3 [see (24)], and it is in some sense an artifact of this model. This artifact, furthermore, makes challenging a direct comparison of the values of the trace shifts δt_p as predicted by models 1, 2 versus model 3. We illustrate this problem by plotting in Fig. 8(a) the time shifts of all the traces as calculated using model 3 (solid lines), as well as time shifts (dotted lines) as computed by model 1 (model 2 gives time shifts virtually identical to those of model 1). We see that because of the nonzeros $\mathrm{mod}(\varphi_{p,r}, 2\pi)$ contributions, the value of the time shifts predicted by the two models is somewhat different. For the rest of the statistical parameters, such as the trace power and the trace phase, we observe an overall excellent correspondence between model 1 and model 3 [see Fig. 8(b) and (c)], however trace-to-trace variation of these parameters is more significant in the case of model 3. This is especially pronounced when comparing the frequency averaged trace noise for the two models [see Fig. 8(d)], which is almost 50% larger for model 3 than for model 1. For model 3, the frequency averaged fit error for trace p is defined as follows:

$$\delta E_p^2 = \frac{1}{N_u}\sum_{r=1}^{N_u}\frac{1}{N_\omega^r}\sum_{n=1}^{N_\omega^r}\left|E_o\left(\omega_n^r\right)\cdot\delta_p\left(\omega_n^r\right)\right|^2. \tag{26}$$

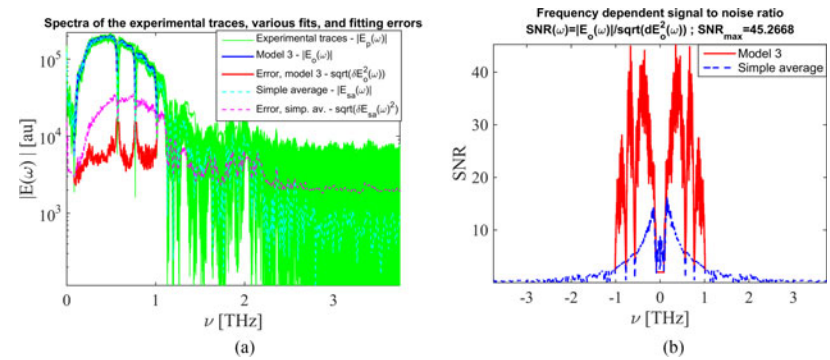

Fig. 9. Comparison of the quality of the fit using model 3 versus a simple average approximation. (a) Spectra of the experimental traces, those of various fits and the corresponding fitting errors. (b) Frequency-dependent signal-to-noise ratio for various fits.

In fact, higher level of noise associated with model 3 compared to model 1 is easy to explain by noting that the number of frequencies used in fitting within model 3 is significantly lower than that used within model 1. This is because in model 3 we use only the frequencies within the common intervals of successful phase unwrapping, which are confined to <1 THz in this particular example (see Fig. 6). At the same time, model 1 uses all the frequencies up to 3.75 THz. As the noise amplitude decreases with the number of frequencies used in the fit, it is not surprising that the results given by model 3 are noisier than those given by model 1.

Finally, in Fig. 9(a), we plot spectra $E_p(\omega)$ of the experimental pulses (solid green), spectrum of the fitted nominal pulse $E_o(\omega)$ (solid blue), and a spectrum of the fitting error $\delta E_o(\omega)$ (solid red) defined as a tracewise average of the individual relative fitting errors $\delta_p(\omega)$ (18) multiplied by the nominal pulse spectrum

$$\delta E_o^2(\omega) = \frac{1}{N_t}\sum_{p=1}^{N_t} \left|E_o(\omega)\cdot\delta_p(\omega)\right|^2. \tag{27}$$

Similar to the results of model 1, we see that the fitting error resulting from model 3 is much smaller than that of the error associated with a simple average approximation. This is especially evident when plotting a frequency-dependent SNR (see Fig. 9 right panel) defined as in (19). Finally, we note that SNR for the fit using model 3 is almost twice as small as that using model 1, which is consistent with the earlier discussion about the noisier nature of model 3.

IX. Conclusion

In this paper, we have first discussed the main types of noise in a typical pump–probe system, and then focused specifically on a THz-TDS setup. Next, we introduced three advanced fitting models for the pulses obtained in such systems, and detailed rigorous mathematical algorithms to find the corresponding fitting parameters. Finally, we performed a comparative analysis of the performance, advantages, and limitations of the three algorithms by testing them on the experimental data collected using a particular THz-TDS system available in our laboratories.

More specifically, in our models we distinguish the "fast" noise, which is considered to be effectively negated by a lock-in amplifier, from the "slow" noise that describes trace-to-trace variations in the pulse power, pulse phase, and pulse spectral position (jitter). While the three fitting models include in the same way effects of the "slow" noise, however, they are different in the way they treat the leftover "fast" noise, which is not completely compensated by a lock-in amplifier. These differences result in three distinct mathematical algorithms that are presented in great details and that feature very different sets of computational advantages and limitations.

Overall, we observe that models 1 and 2 are superior to model 3 in terms of the resultant fitting errors, the overall quality of the fit, and numerical stability. This is related to the fact that model 3 only uses data at frequencies at which phase unwrapping is successful for all the traces, while models 1, 2 use all the frequencies in the pulse spectra. Moreover, even if the phase unwrapping is successful, at the edges of the spectrum, noise contribution to the phases can be significant so that computation of various averages using $\mathrm{mod}(\ldots, 2\pi)$ operation can become unstable. This leads to further limitation on the choice of frequencies that can be used in the fitting procedure and renders model 3 to be somewhat unpredictable in terms of the quality of a fit.

A clear advantage of model 3 compared to models 1, 2 is that it employs only a linear system of equations that can be solved analytically in a closed form. Therefore, computational effort associated with model 3 is significantly smaller than that associated with models 1, 2 which require solution of a system of nonlinear equations.

Finally, another important strength of model 3 is that it gives a properly unwrapped phase of a nominal trace, which can be further used for statistical analysis of signals in more complex algorithms like a cut-back method.

References

[1] F. Raski and K. R. Wilson, "Ultrafast X-ray absorption probing of a chemical reaction," *J. Chem. Phys.*, vol. 104, no. 15, pp. 6066–6069, Apr. 1996.

[2] J. Zhu, X. Wu, D. M. Lattery, W. Zhang, and X. Wang, "The ultrafast laser pump-probe technique for thermal characterization of materials with micro/nanostructures," *Nanoscale Microscale Thermphys. Eng.*, vol. 21, no. 3, pp. 177–198, Apr. 2017.

[3] J. Cabanillas-Gonzalez, G. Grancini, and G. Lanzani, "Pump-probe spectroscopy in organic semiconductors: Monitoring fundamental processes of relevance in optoelectronics," *Adv. Mater.*, vol. 23, no. 46, pp. 5468–5485, Oct. 2011.

[4] M. C. Fischer, J. W. Wilson, F. E. Robles, and W. S. Warren, "Invited review article: Pump-probe microscopy," *Rev. Sci. Instrum.*, vol. 87, no. 46, Mar. 2011, Art. no. 031101.

[5] E. M. Grumstrup, M. M. Gabriel, E. E. M. Cating, E. M. Van Goethem, and J. M. Papanikolas, "Pump-probe microscopy: Visualization and spectroscopy of ultrafast dynamics at the nanoscale," *Chem. Phys.*, vol. 458, pp. 30–40, Sep. 2015.

[6] I. Carrasco-Garcia, J. M. Vadillo, and J. J. Laserna, "Visualization of surface transformations during laser ablation of solids by femtosecond pump-probe time-resolved microscopy," *Spectrochim. Acta B*, vol. 113, pp. 30–36, Aug. 2015.

[7] C. S. Gonçalves *et al.*, "A dual-colour architecture for pump-probe spectroscopy of ultrafast magnetization dynamics in the sub-10- femtosecond range," *Sci. Rep.*, vol. 6, Mar. 2015, Art. no. 22872.

[8] J. A. Moon, "Optimization of signal-to-noise ratios in pump-probe spectroscopy," *Rev. Sci. Instrum.*, vol. 64, pp. 1775–1778, Jul. 1993.

[9] K. E. Anderson, S. L. Sewall, R. R. Cooney, and P. Kambhampati, "Noise analysis and noise reduction methods in kilohertz pump-probe experiments," *Rev. Sci. Instrum.*, vol. 78, Jul. 2007, Art. no. 073101.

[10] P. U. Jepsen and B. M. Fischer, "Dynamic range in terahertz time-domain transmission and reflection spectroscopy," *Opt. Lett.*, vol. 30, no. 1, pp. 29–31, Jan. 2005.

[11] M. Naftaly and R. Dudley, "Methodologies for determining the dynamic ranges and signal-to-noise ratios of terahertz time-domain spectrometers," *Opt. Lett.*, vol. 34, no. 8, pp. 1213–1215, Apr. 2009.

[12] M. Naftaly, "Metrology issues and solutions in THz time-domain spectroscopy: noise, errors, calibration," *IEEE Sens. J.*, vol. 13, no. 1, pp. 8–17, Jan. 2013.

[13] L. Duvillaret, F. Garet, and J.-L. Coutaz, "Influence of noise on the characterization of materials by terahertz time-domain spectroscopy," *J. Opt. Soc. Amer. B, Opt. Phys.*, vol. 17, no. 3, pp. 452–461, Mar. 1996.

[14] T. D. Dorney, R. G. Baraniuk, and D. M. Mittleman, "Material parameter estimation with terahertz time-domain spectroscopy," *J. Opt. Soc. Amer. A, Opt. Image Sci.*, vol. 25, no. 6, pp. 1059–1072, Jun. 2008.

[15] W. Withayachumnankul, B. M. Fischer, H. Liu, and D. Abbott, "Uncertainty in terahertz time-domain spectroscopy measurement," *J. Opt. Soc. Amer. B, Opt. Phys.*, vol. 18, no. 7, pp. 1562–1571, Jul. 2001.

[16] I. Pupeze, R. Wilk, and M. Koch, "Highly accurate optical material parameter determination with THz time-domain spectroscopy," *Opt. Express*, vol. 15, no. 7, pp. 4335–4350, Apr. 2007.

[17] D. R. G. Martin van Exter and D. R. Grischkowsky, "Characterization of an optoelectronic terahertz beam system," *IEEE Trans. Microw. Theory Techn.*, vol. 38, no. 11, pp. 1684–1691, Nov. 1990.

[18] Y. Liang, W. Fan, and B. Xue, "Terahertz TDS signal de-noising using wavelet shrinkage," *Chin. Opt. Lett.*, vol. 9, Jun. 2011, Art. no. S10504.

[19] X. Qiao, X. Zhang, J. Ren, D. Zhang, G. Cao, and L. Li, "Mean estimation empirical mode decomposition method for terahertz time-domain spectroscopy de-noising," *Appl. Opt.*, vol. 56, no. 25, pp. 7138–7145, Aug. 2017.

[20] Y. Chen, S. Huang, and E. Pickwell-MacPherson, "Frequency-wavelet domain deconvolution for terahertz reflection imaging and spectroscopy," *Opt. Express*, vol. 18, no. 2, pp. 1177–1190, Jan. 2010.

[21] B. Ferguson and D. Abbott, "De-noising techniques for terahertz responses of biological samples," *Microelectron. J.*, vol. 32, no. 12, pp. 943–953, Dec. 2001.

[22] B. Ferguson and D. Abbott, "Wavelet de-noising of optical terahertz pulse imaging data," *Fluctuation Noise Lett.*, vol. 1, no. 2, pp. L65–L69, May 2001.

[23] S. P. Mickan, R. Shvartsman, J. Munch, X.-C. Zhang, and D. Abbott, "Low noise laser-based T-ray spectroscopy of liquids using double-modulated differential time-domain spectroscopy," *J. Opt. B, Quantum Semiclassical Opt.*, vol. 6, pp. S786–S795, Jul. 2004.

[24] S. P. Mickan, D. Abbott, and X.-C. Zhang, "Noise Reduction in terahertz thin film measurements using a double modulated differential technique," *Fluctuation Noise Lett.*, vol. 2, no. 1, pp. R13–R28, Apr. 2002.

[25] S. P. Mickan *et al.*, "Thin film characterization using terahertz differential time-domain spectroscopy and double modulation," *Fluctuation Noise Lett.*, vol. 2, no. 1, pp. R13–R28, Apr. 2002.

[26] Z. Jin *et al.*, "Distortion reduction by introducing an initial birefringence in intense terahertz time-domain spectroscopy system," *J. Phys. D, Appl. Phys.*, vol. 50, no. 25, pp. R13–R28, Jun. 2017.

[27] R. Ulbricht, E. Hendry, J. Shan, T. F. Heinz, and M. Bonn, "Carrier dynamics in semiconductors studied with time-resolved terahertz spectroscopy," *Rev. Mod. Phys.* vol. 83, no. 2, pp. 543–586, Apr. 2011.

[28] M. Skorobogatiy, J. Sadasivan, and H. Guerboukha, "Appendix sections to: Statistical models for averaging of the pump-probe time traces: Example of denoising in terahertz time domain spectroscopy," *arXiv: 1711.03566*, Jan. 2018.

[29] M. Skorobogatiy, "PolyFIT-THz code," Nov. 2017. [Online]. Available: http://www.polymtl.ca/phys/photonics/PolyFIT_THz/PolyFIT_THz_code.zip

Maksim Skorobogatiy (SM'17) received the graduate degrees from the Massachusetts Institute of Technology (MIT), Cambridge, MA, USA, in 2001, the M.Sc. degree from the Department of Electrical Engineering and Computer Science, MIT, and the Ph.D. degree in physics from MIT.

He then worked with the MIT spin-off Omniguide Inc. in the capacity of the theory and simulations group leader, on the development of hollow-core fibers for guidance of high-power mid-IR laser beams. He was hired by Polytechnique Montréal, QC, Canada, in 2003, and was awarded a Tier 2 Canada Research Chair (CRC) in Micro and Nano Photonics and then a Tier 1 CRC in Ubiquitous THz Photonics in 2016. Thanks to the support of the CRC program, he could pursue many high-risk exploratory projects in guided optics, and recently THz photonics, which have resulted in significant contributions in these two booming research fields.

Dr. Skorobogatiy became a Fellow of the Optical Society of America for his pioneering contributions to the development of micro structured and photonic crystal multi-material fibers and their applications to light delivery, sensing, smart textiles and arts, in 2017. In 2012, he was bestowed the rank of Professional Engineer by the Order of Engineers of Québec, Canada.

Jayesh Sadasivan received the B.Sc. (Hons.) degree in physics and M.Sc. degree in physics with a specialization in photonics from the Sri Sathya Sai Institute of Higher Learning, Anantapur, India, in 2014 and 2016, respectively.

From 2016 to 2017, he did an international internship on the topic of THz waveguide sensors under the supervision of Prof. Maksim Skorobogatiy with the Ecole Polytechnique de Montréal.

Hichem Guerboukha (GS'17) received the B.Sc. degree in engineering physics and M.Sc. degree in applied science from the Polytechnique Montréal, Montréal, QC, Canada, in 2014 and 2015, respectively. He is currently working toward the Ph.D. degree in THz computational imaging.

His research interests include THz instrumentation and waveguides, THz communications, and THz computational imaging.

Mr. Guerboukha was the recipient of the Étoile Student-Researcher from Fonds de recherche–Nature et technologies in 2015 and the Best M.S. Thesis Prize from the Polytechnique Montréal in 2015.